PHOTONICS Research

Surface-enhanced Raman scattering on dielectric microspheres with whispering gallery mode resonance

STEVEN H. HUANG,[1] (iD) XUEFENG JIANG,[1] BO PENG,[1] COREY JANISCH,[2] ALEXANDER COCKING,[2]
ŞAHIN KAYA ÖZDEMIR,[1] ZHIWEN LIU,[2] AND LAN YANG[1],*

[1]Department of Electrical and Systems Engineering, Washington University in St. Louis, St. Louis, Missouri 63130, USA
[2]Department of Electrical Engineering, Pennsylvania State University, University Park, Pennsylvania 16802, USA
*Corresponding author: yang@seas.wustl.edu

Conventionally, metallic nanostructures are used for surface-enhanced Raman spectroscopy (SERS), but recently there has been increasing interest in the enhancement of Raman scattering from dielectric substrates due to their improved stability and biocompatibility compared with metallic substrates. Here, we report the observation of enhanced Raman scattering from rhodamine 6G molecules coated on silica microspheres. We excite the whispering gallery modes (WGMs) supported in the microspheres with a tapered fiber coupler for efficient WGM excitation, and the Raman enhancement can be attributed to the WGM mechanism. Strong resonance enhancement in pump laser intensity and modified Raman emission from the Purcell effect in the microsphere resonator are observed from the experiment and compared with theoretical results. A total Raman enhancement factor of 1.4×10^4 is observed, with contribution mostly from the enhancement in pump laser intensity. Our results show that, with an efficient pumping scheme, dielectric microspheres are a viable alternative to metallic SERS substrates. © 2018 Chinese Laser Press

1. INTRODUCTION

Whispering gallery mode (WGM) microresonators, such as microspheres and microtoroids, have attracted much interest for their potential application in label-free sensing of biomolecules, nanoparticles, and chemicals [1,2]. These resonators have ultra-high quality (Q) factors and small mode volumes, allowing for greatly enhanced light–matter interaction and high sensitivity to adsorbed analytes. Label-free, single particle level sensitivity to virus particles, proteins, nucleic acids, and even single ions has been demonstrated [3–9]. Currently, the sensing schemes are based on observing the change in the transmission spectrum of the resonator, appearing as either shift, splitting, or broadening of the resonance mode [7,8,10]. In essence, all of these sensing schemes measure the polarizability of the analyte, and WGM resonator sensors lack specificity beyond distinguishing entities with different polarizabilities. Although sensing specificity can be added to the system by surface functionalization, a complementary method to WGM sensing that can provide molecular fingerprints of the analyte without functionalization is desirable.

Raman spectroscopy is a widespread analytical technique that can be used for material identification without labeling or functionalization. Raman scattering is typically a weak process, but the introduction of surface-enhanced Raman scattering (SERS) has greatly improved the detection limit of Raman spectroscopy. In SERS, the analyte is placed on nanostructured metallic surfaces or metallic nanoparticles, typically made of coinage metals such as Au, Ag, and Cu, and the plasmonic "hotspots" produced by these metallic structures are used to enhance the Raman signal. A large enhancement factor on the order of 10^{10} to 10^{12} has been reported from SERS, making Raman detection of single molecules possible [11–13].

Large field enhancement, however, is not unique to plasmonic structures alone. Recently, the use of dielectric and semiconductor micro/nanostructures as a SERS substrate has received increasing attention [14–27]. These dielectric and semiconductor substrates, typically made of SiO_2, Si, or TiO_2, have several advantages over metallic SERS substrates. Dielectric SERS substrates are more stable under high-temperature and harsh electrochemical conditions [21,27],

leading to a more repeatable SERS enhancement. Dielectrics also have reduced perturbation of the analyte both chemically and thermally [28,29]. In particular, the local heating of metallic nanostructures upon optical pumping can be significant [30], which can adversely affect the SERS substrate [31] and the analyte [29]. It has been shown that, in dielectric nanostructures, this heating can be negligible [15].

Dielectric SERS substrates can come in many forms, with microspheres or 2D/3D arrays of microspheres as one of the most popular forms. However, the exact mechanism for Raman enhancement in these dielectric microspheres is still not completely understood, due to the complexity that arises from the interplay among the many mechanisms involved [14]. Several enhancement mechanisms have been identified so far, with the most studied electromagnetic effects being photonic nanojets and WGM resonances, often also called morphology-dependent resonances in this context. Photonic nanojets are nonevanescent and nonresonant beams of light with enhanced field intensity, which are formed on the shadow side of the microspheres when the microspheres are illuminated from above. Due to the focusing of pump light at the nanojet, Raman signal from a sample under the microsphere is enhanced, typically by approximately a factor of 10–100 [16–20]. WGM resonances in these microspheres, on the other hand, are theoretically predicted to have Raman enhancement up to 10^8, comparable with metallic SERS substrates [32,33], but experimental demonstration of Raman enhancement from WGMs in dielectric microspheres has been limited and inconclusive thus far [17,21,22]. Other Raman enhancement mechanisms identified in arrays of microspheres and inverse opal structures include Fabry–Perot effects [17], photonic bandgap effects [23], and directional antenna effects [24]. Also, chemical enhancement attributed to charge transfer complexes is often observed from semiconductor substrates, such as TiO_2 and ZnO [25,26].

The difficulty in studying WGM enhancement mechanisms in microspheres mainly arises from the inefficiency in pumping the WGMs with a conventional micro-Raman spectroscopy setup, which is often designed for a conventional Raman signal or SERS signal from metallic substrates [13]. In dielectric microspheres, the linewidth of a typical WGM resonance is much narrower than that of plasmonic resonances in metallic nanostructures. In addition, these narrow WGMs often shift by more than their linewidths upon analyte adsorption or photothermal heating due to the pump light. Thus, although a fixed-wavelength excitation laser is suitable for pumping the broad plasmonic resonances, pumping the narrow and fluctuating WGMs poses a significant challenge. Further, because the dielectric microspheres that support WGMs are larger than the wavelength of excitation light, phase matching between the excitation beam and the WGMs can no longer be ignored, as in the case for plasmonic resonances from metallic nanoparticles. This leads to inefficient coupling of light from the free-space beam to WGMs, even when the wavelengths are matched. Inefficient coupling to WGMs from these factors often results in the effect of WGM enhancement being masked by other phenomena.

In this work, we study the WGM Raman enhancement mechanism by pumping a single silica microsphere through a tapered fiber coupler using a narrow-linewidth tunable laser. Tapered fiber couplers can couple more than 99% of the pump light into a single WGM in ideal conditions [34] and therefore have been routinely used for experiments with WGM resonator based sensors and microlasers [3,35]. By using a tapered fiber coupler to pump a single microsphere, we also avoid other electromagnetic effects in microspheres such as photonic nanojets. In addition, the use of a silica microsphere excludes the contribution of chemical enhancement. Thus, the entire Raman enhancement can be attributed to the WGM mechanism. From our result, we observed a clear enhancement of Raman scattering and modified Raman emission spectra due to WGMs. Our work demonstrates that significant Raman enhancement is possible using the same platform as that for WGM sensors, allowing for the two techniques to complement each other; Raman spectroscopy provides added molecular specificity to WGM resonator-based sensors, while the WGM resonator enhances the strength of the Raman signal.

2. EXPERIMENTAL METHODS

A. Fabrication of the Silica Microsphere

Silica microspheres were fabricated on a silicon chip, with each microsphere supported by a silicon "pillar" [36–38]. Briefly, circular silica disks were lithographically defined and etched with HF. XeF_2 etching was used to undercut the circular disks, such that most of the disks were suspended in air, with only a small portion supported in the center by the silicon pillar. A subsequent irradiation by a CO_2 laser reflowed the silica disk into a small microsphere (Fig. 1 inset).

B. Optical Setup

We used an in-house-built Raman spectrometer to collect the Raman emission from the microsphere, a schematic drawing of which is shown in Fig. 1. A fiber-coupled external cavity tunable laser (765–781 nm) was used to excite the WGM resonances. As the pump light travels through the fiber, it excites Raman scattering from the silica fiber, which can interfere with the Raman signal from the microsphere. An 800 nm short-pass filter was used to remove this contribution. After this filter, the pump light propagates through a tapered fiber, which was
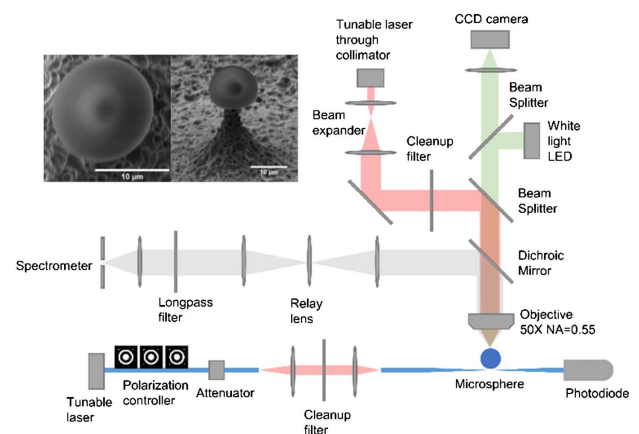

Fig. 1. Schematic of the experimental setup. Inset: top view (left) and side view (right) of a typical on-chip microsphere used in the experiment.

coupled with the microsphere. Finally, the transmitted light through the tapered fiber coupler was measured using a photodiode to monitor the coupling of the pump light to WGMs in the microsphere.

The Raman emission from the microsphere was collected from the top by a long working distance objective (NA = 0.55). The objective was also used for imaging the microsphere resonator. In order to separate the Raman emission collection path from the imaging path, an 805 nm dichroic mirror was used. An 800 nm long-pass filter was used to remove the Rayleigh scattered pump laser, after which the Raman emission spectrum was recorded using a grating spectrometer.

A free-space excitation path was included in the setup to compare the tapered fiber excitation with conventional free-space excitation of Raman scattering. The same tunable laser was used for excitation; this laser was coupled to free space through a collimator, and a beam expander was used to adjust its beam size. A cleanup filter was used to remove the Raman emission generated in the fiber. The pump laser was focused on the microsphere through the same objective used for imaging.

For pumping with a tapered fiber coupler, the chip with a microsphere was mounted vertically on its side, and the light scattered from the WGMs was collected with the optical axis of the collection objective in the equatorial plane of the microsphere. Because most of the light from the microsphere is scattered in the equatorial plane due to radiation loss, this collection scheme is more efficient than collecting light scattered perpendicular to the equatorial plane. For free-space pumping, the chip was placed horizontally, so that the pump light was incident on the microsphere from the top.

C. Rhodamine 6G Coating

To study the microsphere's Raman enhancement for surface-adsorbed molecules, we coated the surface of the microsphere with rhodamine 6G and studied the enhancement of its Raman scattering. 1 µL of 5 mg/mL rhodamine 6G solution in ethanol was dropped onto the chip with the microsphere and was dried in air [21]. The resonance wavelength of the pump WGM was measured before and after rhodamine 6G coating. From the shift in the WGM's resonance wavelength, we estimated the thickness of rhodamine 6G on the microsphere to be 3.4 nm. The thickness of the rhodamine 6G layer on the substrate was estimated to be 200 nm based on the amount of rhodamine 6G deposited and was confirmed with a scanning electron microscope (SEM) measurement (image not shown). This large difference in the amount of analyte being pumped is important in calculating the enhancement factor, and being able to measure the amount of rhodamine 6G molecules on the microsphere through WGM resonance wavelength shift is a significant advantage in our system.

3. RESULTS AND DISCUSSION

Raman lasing in silica microsphere and microtoroid resonators is a well-known effect [35,39], but the occurrence of a Raman laser is detrimental for our work in Raman spectroscopy in two ways. First, the contribution from significant stimulated emission makes our estimate of Raman enhancement factor highly inaccurate. Second, any Raman laser in the microsphere may

cause cascaded Raman lasing, which acts as secondary pumps that distort the measured Raman spectrum. To ensure there is no contribution from Raman lasing, we first characterized the lasing threshold in our microspheres, the result of which is shown in Fig. 2(a). The Raman lasing threshold was identified to be around 200 µW; for the subsequent experiments, the pump power was kept to below 100 µW to avoid contribution from stimulated Raman scattering. The inset in Fig. 2(a) shows the subthreshold portion of the Stokes light intensity; this part has linear dependence on pump power, as expected from spontaneous Raman scattering.

We first excited Raman scattering in a bare silica microsphere to characterize the effect of WGM resonance on silica Raman scattering. A microsphere with a diameter of 13.8 µm
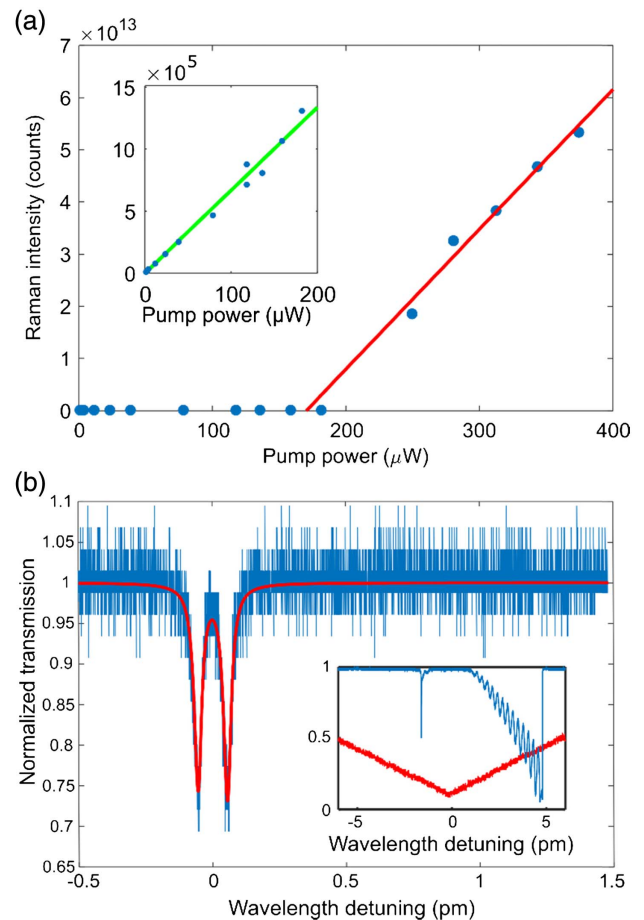

Fig. 2. Raman lasing and thermal effects in silica microspheres. (a) Raman intensity dependence on pump power for a bare silica microsphere. Inset shows the linear dependence of Raman intensity on pump power in the spontaneous Raman emission regime. (b) Measured transmission spectrum through the fiber taper coupler around a typical WGM resonance. Inset shows the transmission spectrum (blue curve) of the same modes at a higher power typically used for Raman pumping, with significant thermal broadening. The red triangular waveform corresponds to the scanning of the pump laser wavelength; the left half corresponds to a decreasing pump wavelength, while the right half corresponds to an increasing pump wavelength. The oscillation seen in the thermally broadened WGM is due to interference effect from reflection at fiber ends, which is unrelated to the WGM resonance.

and a WGM at 767.54 nm with an intrinsic Q-factor of 2×10^7 was used for this measurement [Fig. 2(b)]. The resonance mode is split into two due to the coupling of clockwise and counterclockwise traveling wave modes. At high power, there was strong thermal broadening in the observed transmission spectrum of the WGM, as presented in the Fig. 2(b) inset. This broadening arises due to the shift in the resonance wavelength caused by the heat generated by the pump light, and several picometers of resonance wavelength shift are observed regularly even for modest pump power (few tens of μW) [40]. This suggests that, without a tunable laser and active monitoring of the WGM, it is difficult to couple a high-intensity pump light efficiently into the WGM because, as soon as the pump light is coupled in, the WGM shifts, reducing its spectral overlap with the pump light. In our experiment, we keep the pump light scanning across the WGM during Raman signal collection and calculate from the transmission spectrum the fraction of pump power coupled into the resonator on average (typically 0.2–0.5, see Appendix A); this fraction is accounted for when we compare the Raman intensity from different spectra. Although the pump efficiency is not ideal, we find that this method results in a stable and quantifiable coupling of the pump power into the WGM over the spectrometer's integration time.

Figure 3(a) presents the observed Raman emission from the silica microsphere with pump light on resonance with a WGM. The spectrum consists of a broad background that corresponds to the Raman features of bulk silica as well as numerous sharp peaks. These sharp peaks are the result of the modified density of states from WGM resonance (i.e., the Purcell effect); each of these peaks corresponds to a WGM of the microsphere resonator, with a periodicity that agrees with the calculated free

(a)

(b)

(c)

Fig. 3. Raman emission from a bare silica microsphere. (a) Integrated Raman spectrum from a 13.8 μm silica microsphere. (b) Raman spectra from different positions in the microsphere. Red dotted circles in the inset indicate the positions from which the spectra were collected. (c) Measured Raman intensity dependence on pump detuning. Red curve shows a Lorentzian fit to the experimental data.

spectral range. Due to slight eccentricity of the microsphere, we have eccentricity-induced splitting, and the WGMs appear in several "groups" of closely spaced modes [39]. The WGM peaks correspond to the Raman emission from silica that is first emitted into the WGMs and then scattered to free space to be collected by the objective. On the other hand, the broad background corresponds to the Raman emission that is not coupled to WGMs but instead emitted directly into free space. As a result, there is a notable spatial variation in the Raman emission from the silica microsphere, as shown in Fig. 3(b); the WGM peaks are much more prominent at the two edges of the resonator than at the center of the resonator, indicating that these peaks correspond to the light lost from the WGMs due to the perturbed total internal reflection from the curvature of the microsphere. Also, this emission pattern indicates that the emission from the two sides of the resonator is approximately equal. This confirms that Raman scattering has equal intensity in the forward scattering and backward scattering directions.

With this silica microsphere resonator, we have investigated the dependence of Raman intensity on the wavelength detuning of the pump from a resonance [Fig. 3(c)]. There is a large enhancement in the collected Raman signal when the pump is on resonance with a WGM. This enhancement can be mostly attributed to the power enhancement of the pump light in the resonator. At critical coupling, the power enhancement is [41]

$$B = \frac{P_{\text{cavity}}}{P_{\text{incident}}} = \frac{1}{2\pi} \frac{\Delta\lambda_{\text{FSR}}}{\Delta\lambda_{\text{FWHM}}} \frac{1}{1 + \left(\frac{\Delta\lambda}{\Delta\lambda_{\text{FWHM}}}\right)^2}, \quad \textbf{(1)}$$

where $\Delta\lambda$ is the wavelength detuning of the pump light, $\Delta\lambda_{\text{FSR}}$ is the free spectral range of the optical cavity, and $\Delta\lambda_{\text{FWHM}}$ is the linewidth of the optical mode. For our resonator, we have $\Delta\lambda_{\text{FSR}} = 10.5$ nm and $\Delta\lambda_{\text{FWHM}} = 0.12$ pm, resulting in $B = 1.4 \times 10^4$ at zero detuning. To compare this value to the one obtained in our experiment, we note that, at the detuning of $\Delta\lambda = (\frac{1}{2\pi}\Delta\lambda_{\text{FWHM}}\Delta\lambda_{\text{FSR}})^{\frac{1}{2}} = 0.014$ nm, we have $P_{\text{cavity}} = P_{\text{incident}}$. Thus, by taking the ratio of the peak Raman intensity at zero-detuning and at 0.014 nm detuning, we obtain the experimentally measured Raman enhancement to be 4.9×10^3, in good agreement with the theoretically predicted value. The discrepancy between the two can be attributed to the nonideal pumping at zero detuning and the contribution of background light in the Raman spectra for detuned pump, where the Raman signal is low.

In calculating the above theoretical enhancement factor, we have ignored the contribution from the Purcell effect, which clearly modifies the Raman spectrum and causes the sharp peaks to appear. Because the Raman spectrum of silica is broad and spans over several free-spectral ranges, we expect little enhancement in the total power of the emitted Stokes light due to the Purcell effect [33,42]. However, within the linewidth of a particular WGM, the Purcell enhancement in the Raman spectral density is significant. The enhancement in Raman spectral density can be estimated by integrating the background-subtracted intensity within a WGM peak, dividing it by the linewidth of the WGM, and comparing the result to the silica background Raman intensity. It is important to note here that the width of WGM peaks in the Raman spectrum is limited by the spectrometer and is not the true linewidth; instead,
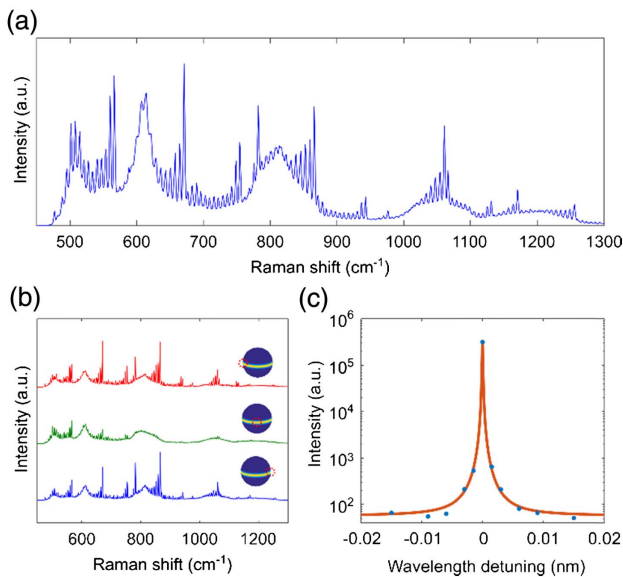
we assume the linewidth of the Stokes WGM to be the same as the pump mode, at $\Delta\lambda_{\mathrm{FWHM}} = 0.12$ pm. From this, we estimate the spectral density enhancement within a WGM due to the Purcell effect to be 6.8×10^3.

Next, we studied the enhancement of the Raman signal from rhodamine 6G molecules coated on the surface of a silica microsphere. We compared the Raman spectra from rhodamine 6G excited in three different ways. The first is the excitation of rhodamine 6G on a microsphere that is resonantly pumped through a tapered fiber coupler, as previously described for the bare silica microsphere. The second is the excitation of rhodamine 6G on the substrate near the microsphere with a free-space Gaussian beam, with an estimated beam diameter of 7 μm. This measurement serves as a control where no Raman enhancement due to the microsphere is present. The third is the free-space beam excitation of the rhodamine 6G on the microsphere, which serves as a comparison with previously published results on microsphere-based Raman enhancement with conventional micro-Raman setups [17–21]. The excitation beam is directed onto the rhodamine 6G coated microsphere from the top in this third case.

The observed Raman spectra for rhodamine 6G on the microsphere is presented in Fig. 4(a). Another microsphere with a diameter of 17.3 μm was used for this measurement. The pump wavelength was 769 nm for pumping with a tapered fiber coupler and 770 nm for free-space pumping. The modified Raman emission due to the Purcell effect is only visible for the microsphere pumped by the fiber taper. This can be attributed to the higher WGM coupling efficiency from the tapered fiber pumping; the Stokes light only couples to a WGM when the Raman scatterer has spatial overlap with the Stokes WGM, and this coupling is more efficient when the pump light is also in a WGM. For the peak at 1510 cm^{-1}, there are two sharp peaks from tapered fiber pumping but only one broad peak, which corresponds to the bulk Raman spectrum, from free-space pumping of the microsphere or the substrate. This can be attributed to the modified Raman emission in the presence of an optical cavity; two WGMs overlap with the Raman peak at 1510 cm^{-1}, and there is selective enhancement of Raman scattering at the resonance wavelengths of these two WGMs, leading to what looks like two peaks. By comparing the integrated area of the rhodamine 6G peak at 1510 cm^{-1} over a spectral band of 24 cm^{-1}, we find the Raman intensity from the tapered fiber pumped microsphere to be larger than the Raman intensity from rhodamine 6G on the substrate by a factor of 928. Similarly, we find the Raman intensity for the free-space pumped microsphere to be seven times larger than the Raman intensity from rhodamine 6G on the substrate, which is in agreement with previously published results [16–19]. Free-space pumping is expected to have little coupling to WGMs, and the enhancement in Raman intensity from free-space pumping of the microsphere is expected to be mostly due to the photonic nanojet effect. Our results clearly show that the enhancement from WGMs can be much higher than that from a photonic nanojet.

From the spectra in Fig. 4(a), we can identify two mechanisms for the Raman enhancement: the pump enhancement, which uniformly increases the Raman intensity at all Stokes
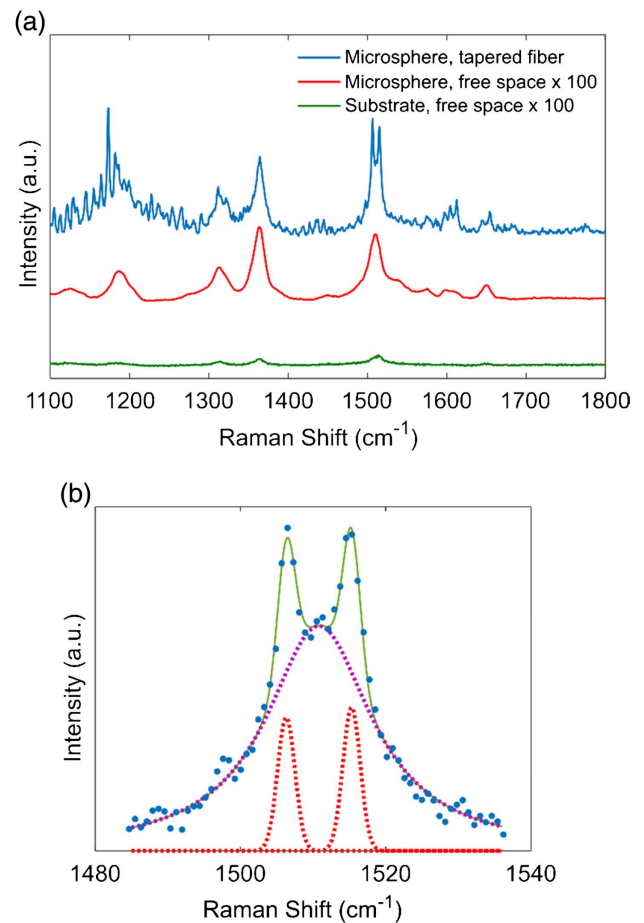

Fig. 4. Raman enhancement of rhodamine 6G through the silica microsphere. (a) Background subtracted Raman spectra of rhodamine 6G for tapered fiber coupler excitation (blue), free-space excitation on a microsphere (red), and free-space excitation on the substrate (green). The spectra for free-space excitation on the microsphere and substrate are scaled by 100 times for visibility. (b) Raman spectrum of rhodamine 6G around the 1510 cm^{-1} peak, obtained from subtracting the spectrum after photobleaching from the spectrum before photobleaching. The solid green curve is a fit to the data points. The spectrum is fitted as sum of a Lorentzian Raman peak (purple dotted curve) and two Gaussian WGM peaks (red dotted curve).

wavelengths, and the Purcell enhancement, which results in enhancement at Stokes wavelengths matching WGMs only, resulting in Raman spectra modified by sharp resonance peaks. The total Raman enhancement can be approximated as $F_{\mathrm{total}} = F_{\mathrm{pump}} \times (1 + F_{\mathrm{Purcell}})$. This is analogous to the electromagnetic mechanism in SERS, in which, approximately a factor of $[|E_{\mathrm{local}}(\omega_{\mathrm{pump}})|/|E_0(\omega_{\mathrm{pump}})|]^2$ is attributed to pump enhancement, and another factor of $[|E_{\mathrm{local}}(\omega_{\mathrm{Stokes}})|/|E_0(\omega_{\mathrm{Stokes}})|]^2$ is attributed to radiation enhancement resulting in a total of $[|E_{\mathrm{local}}(\omega_{\mathrm{pump}})|/|E_0(\omega_{\mathrm{pump}})|]^4$ enhancement when the Stokes shift is small [11,13]. In what follows, we consider these two enhancement mechanisms in silica microsphere separately and provide a theoretical estimate of the enhancement factors due to each mechanism. We follow the theoretical analysis in recent works on the Purcell-enhanced Raman scattering in Fabry–Perot optical microcavities [43–46].

The pump enhancement factor for molecules adsorbed on the surface of a microsphere can be calculated from the power enhancement factor, as previously discussed, with correction terms that account for the local electric field strength at the surface of the microsphere, the thickness of rhodamine 6G on the microsphere and that on the substrate, and the reduced pump efficiency due to laser scanning. In the pump enhancement factor (F_{pump}), we include these factors that affect the effective pump intensity leading to a spectrally uniform scaling of the Raman intensity, i.e., the factors that do not distort the shape of the original spectrum. The pump enhancement factor can be expressed as

$$F_{pump} = \frac{P_{Raman,WGM}}{P_{Raman,fs}}$$
$$= \frac{V_{R6G,WGM}}{V_{R6G,fs}} \frac{A_{fs}}{A_{WGM}} \frac{1}{2\pi} \frac{\Delta\lambda_{FSR}}{\Delta\lambda_{FWHM}} \eta_{pump}, \qquad (2)$$

where $V_{R6G,WGM} = 0.056\ \mu m^3$ and $V_{R6G,fs} = 4\ \mu m^3$ are the effective volumes of rhodamine 6G being excited by WGM [47] and free-space pumping, respectively, $A_{WGM} = 0.817\ \mu m^2$ is the cross-sectional area of the WGM, $A_{fs} = 20\ \mu m^2$ is the effective cross-sectional area of the free-space pump beam, and $\eta_{pump} = 0.47$ is a correction factor to account for the reduced pump efficiency from the scanning pump laser. This microsphere with rhodamine 6G coating has $\Delta\lambda_{FSR} = 8.4$ nm and $\Delta\lambda_{FWHM} = 0.18$ pm. For our experiment with the spectrum shown in Fig. 4, we obtain $F_{pump} = 1204$. The details of this calculation are presented in Appendix A.

In addition to pump enhancement, Raman emission is also enhanced by the increased density of state due to resonance, characterized by the Purcell factor. Whereas the pump enhancement results in a uniform enhancement of the entire Raman spectrum, the Purcell enhancement only enhances the Raman spectral density within the linewidth of a WGM and thus is highly nonuniform, introducing sharp peaks in the Raman spectra. The Purcell enhancement factor, however, is calculated for the enhancement of total Raman intensity for a particular Raman peak and, thus, is much smaller than the enhancement of Raman spectral density within each WGM linewidth. The ideal Purcell factor is often written as $F_{Purcell,0} = \frac{3}{4\pi^2} \lambda_s^3 \frac{Q_c}{V_s}$, where Q_c is the cavity Q-factor, and V_s is the mode volume of the Stokes WGM [48,49]. Several corrections are required in applying this Purcell factor to our experiment. First, there is a $1/n_s^2$ correction to the Purcell factor due to the optical cavity having a refractive index $n_s = 1.45$ rather than being in vacuum. Second, WGMs typically have narrower linewidth than Raman peaks, which leads to nonuniform enhancement in Raman scattering throughout the Raman peak. Instead of Q_c, the effective increase in the total emitted power over the entire Raman peak is characterized with an effective Q-factor $Q_{eff} = \frac{Q_c Q_R}{Q_c + Q_R}$, with Q_R defined as $Q_R = \frac{\lambda_s}{\Delta\lambda_R}$, where $\Delta\lambda_R$ is the linewidth of the Raman peak [43]. Also, the derivation of Q_{eff} assumes there is a single WGM at the center of the Raman peak, but in practice there may be multiple WGMs that overlap with the Raman peak with some detuning. This spectral overlap between WGM and Raman peak is accounted for by introducing η_λ. Third, the ideal Purcell factor assumes that the emitter lies at the maximum of the cavity field,

but this is not true for microspheres supporting WGMs. Thus, we need to correct for the local electric field strength at the surface of the microsphere, where the rhodamine 6G molecules are, as well as the overlap between the pump WGM and the Stokes WGM. This is accounted for by η_E. Fourth, the Purcell-enhanced Raman scattering is emitted into the Stokes WGM first and then scattered into free space; this emission has a different emission pattern compared with that of Raman scattered light emitted directly into free space. As a result, the fraction of light collected by the objective is different for each type of emission, and we introduce η_Ω to account for this difference in collection efficiency. Fifth, there is a twofold degeneracy in mode density due to the microsphere having both clockwise and counterclockwise WGM, which doubles the Purcell-enhanced Raman emission. Last, some of the light in the Stokes WGM is coupled into the fiber taper and is not collected from the microscope objective. We assume critical coupling to the Stokes mode; in this case, half of the Stokes light is lost through the fiber taper, thus reducing the collected Raman signal by a half. Combining these effects, we obtain

$$F_{Purcell} = \frac{3}{4\pi^2} \frac{\lambda_s^3}{n_s^2} \frac{Q_{eff}}{V_s} \eta_\lambda \eta_E \eta_\Omega \times 2 \times 0.5. \qquad (3)$$

We evaluate the Purcell enhancement factor for the Raman spectrum presented in Fig. 4(a), with $\lambda_s = 0.8743\ \mu m$, $n_s = 1.45$, $Q_{eff} = 640$, $V_s = 49.1\ \mu m^3$, $\eta_\lambda = 1.58$, $\eta_E = 0.17$, and $\eta_\Omega = 1.5$ to obtain $F_{Purcell} = 0.127$. Details of this calculation are presented in Appendix B.

To compare the theoretical results to the experiment, we performed curve fitting to the experimentally obtained Raman spectra to estimate the contribution of the Purcell enhancement in the total Raman enhancement. This is possible because the Purcell enhancement appears as sharp lines that are clearly distinguishable from the bulk Raman spectrum. However, to determine the Purcell enhancement accurately, we need a Raman spectrum corresponding to only that of rhodamine 6G, without any background contribution from silica. In order to obtain such a spectrum, we noted that, as we pump the rhodamine 6G coated microsphere, the Raman peaks of rhodamine 6G gradually decreased and eventually disappeared, likely due to photobleaching of the dye (Appendix C). The difference in the Raman spectrum of a freshly coated microsphere and that of a microsphere pumped for a long time corresponds to the Raman spectrum from rhodamine 6G alone without any silica contribution [Fig. 4(b)]. In performing the curve fitting, the bulk Raman peak was assumed to have a Lorentzian lineshape, whereas the two WGMs had spectrometer-limited linewidth and were fitted with Gaussians. By comparing the integrated areas of the bulk Raman peak and the two WGM peaks, we estimated the Purcell enhancement to be 0.134. This measured Purcell enhancement is in very good agreement with the theoretically calculated value of 0.127. Further, we can also calculate the experimentally measured F_{pump} to be 818. This is also in good agreement with the theoretically calculated value of 1204.

Finally, the Raman enhancement factor of the silica microsphere as an SERS substrate is evaluated as

$$EF = \frac{I_{SERS}/N_{SERS}}{I_0/N_0}, \qquad (4)$$

where I_{SERS} and I_0 are the Raman signal intensity in the SERS and non-SERS spectra, and N_{SERS} and N_0 are the effective number of molecules being excited in the SERS and non-SERS measurement [12]. Here, $\frac{I_{SERS}}{I_0} = F_{total} = 928$, and the ratio $\frac{N_{SERS}}{N_0} = 0.065$ is calculated from the effective volume of rhodamine 6G excited in each pumping scheme (Appendix D). From this, we obtain $EF = 1.4 \times 10^4$. Within this, a minor factor of 1.134 can be attributed to the Purcell enhancement, with the remaining 1.2×10^4 attributed to pump enhancement.

4. CONCLUSION

In conclusion, we have measured the enhanced Raman emission of silica and rhodamine 6G due to WGM resonances in silica microspheres. Our use of a tapered fiber coupler allows us to couple pump light to the WGMs with high efficiency, leading to a higher enhancement factor than is possible with free-space pumping. We estimated the Raman enhancement factor as 1.4×10^4, with most of the enhancement originating from the pump enhancement and a small factor of 1.134 from the Purcell enhancement. These experimentally measured results are in good agreement with theoretical calculations.

The experimentally observed enhancement factor in this work is, to the best of our knowledge, the largest reported from dielectric microspheres so far but still several orders lower than predicted in theory [32,33], which can be as high as 10^8. The largest contributing factor that leads to this smaller experimentally measured enhancement factor is the large linewidth of the rhodamine 6G Raman peak, with $\Delta\lambda_R = 18$ cm^{-1}, compared with that of the Stokes WGM, with linewidth on the order of 0.01 cm^{-1}. Because the Raman peak linewidth is different for different molecules, this factor is often not included in theoretical calculations of the enhancement factor, making the enhancement factor predicted from theory larger than what is attainable for common Raman probes. On the other hand, for some gas phase molecules such as CO_2, the Raman peaks can be much narrower and comparable with WGMs in linewidth [44]. These molecules would result in a much larger enhancement factor from WGMs, predominantly due to an increase in Purcell enhancement. Also, cavity resonance scanning techniques similar to those demonstrated for Fabry–Perot cavities may allow us to obtain a higher Purcell enhancement by scanning the Stokes WGM across the Raman peak [44–46].

An interesting question to consider here is whether dielectric microspheres as SERS substrates have the potential to detect single-molecule Raman spectra. Despite earlier works that have taken single-molecule SERS as an indication for extremely high enhancement factors, it has been recently demonstrated that, when Raman probes with a large cross section such as rhodamine 6G are pumped at their molecular resonance, a single-molecule EF as low as 10^6 is sufficient to observe single molecule SERS [50]. Considering this result, we believe that single-molecule SERS is attainable with dielectric microspheres with some optimization. First, we note that, without any rhodamine 6G coating, a Q-factor above 10^7 is easily achievable with bare silica microspheres. For single-molecule studies,

the perturbation to the WGM would be minimal, and we do not expect any lowering of the Q-factor from that of a bare silica microsphere. The increased Q-factor alone would increase the EF by more than an order of magnitude. Also, for single molecules there is no inhomogeneous broadening [51], leading to a narrower Raman peak and an increased Purcell enhancement from WGMs. Together, with further optimization in the size and refractive index of the microsphere, we believe that a single-molecule EF of 10^6 is realistic for dielectric microspheres supporting WGMs. Although challenges such as the suppression of Raman lasing remains, the demonstration of single-molecule SERS from dielectric microspheres would allow for the probing of molecular dynamics and interactions at previously unattainable levels of details.

A unique advantage of our system, not fully exploited in this work, is the ability to quantitatively measure the number of molecules adsorbed onto the microsphere from a resonance wavelength shift and collect the Raman spectra from the same molecules. Wavelength shift provides another measurement of the number of molecules being excited, independent from Raman spectroscopy. This allows for more accurate quantification of the enhanced Raman spectra. On the other hand, molecular identification through Raman spectroscopy adds otherwise unavailable specificity to the WGM sensing method. This combination of two detection methods can potentially be much more powerful in chemical and biological sensing compared with each method used alone.

APPENDIX A: CALCULATION OF THE PUMP ENHANCEMENT FACTOR

For a single Raman scatterer, the power of the Raman scattered light can be expressed as $P_{Raman} = \sigma_{Raman}S_{local}$, where σ_{Raman} is the Raman cross section and S_{local} is the local power density [52]. Note that here we consider the "total" Raman cross section instead of the differential Raman cross section and ignore its direction-dependence for simplicity. For multiple scatterers, the total Raman scattered power is the sum of the scattered power from each. For our experiment with rhodamine 6G, we have $P_{Raman} = \rho_N \sigma_{Raman} \int_{R6G} S_{local} dV$, where ρ_N is the number density of rhodamine 6G molecules, and the integration is on the volume of rhodamine 6G only. In the case of WGM pumping of the microsphere, the integral $\int_{R6G} S_{local} dV$ can be written as $\int_{R6G} S_{local} dV = \frac{V_{R6G,WGM}}{A_{WGM}} P_{in} \frac{1}{2\pi} \frac{\Delta\lambda_{FSR}}{\Delta\lambda_{FWHM}} \eta_{pump}$, where $V_{R6G,WGM} = \int_{R6G} \frac{\epsilon_p(r)|E_p(r)|^2}{max(\epsilon_p(r)|E_p(r)|^2)} d^3r$, with the integral on the volume of rhodamine 6G only, $A_{WGM} = \int \frac{\epsilon_p(r)|E_p(r)|^2}{max(\epsilon_p(r)|E_p(r)|^2)} d^2r$, with the integral on the cross section of the WGM in the microsphere, P_{in} is the incident power, the factor $\frac{1}{2\pi} \frac{\Delta\lambda_{FSR}}{\Delta\lambda_{FWHM}}$ is the power-enhancement factor from resonance at zero detuning and critical coupling, and the factor η_{pump} accounts for the time-dependent detuning of the scanning laser. Thus, we obtain $P_{Raman,WGM} = \rho_N \sigma_{Raman} \frac{V_{R6G,WGM}}{A_{WGM}} P_{in} \frac{1}{2\pi} \frac{\Delta\lambda_{FSR}}{\Delta\lambda_{FWHM}} \eta_{pump}$. Note that the product $\rho_N V_{R6G,WGM}$ can be considered as the effective number of molecules excited by the WGM, and we use this

term later to compare the number of molecules excited by WGM pumping and free-space pumping.

For free-space pumping, we start from $P_{\text{Raman}} = \rho_N \sigma_{\text{Raman}} \int_{\text{R6G}} S_{\text{local}} dV$ again but use the free-space beam profile for S_{local}, assuming a Gaussian beam profile for the free-space pump light. We obtain $P_{\text{Raman,fs}} = \rho_N \sigma_{\text{Raman}} \frac{V_{\text{R6G,fs}}}{A_{\text{fs}}} P_{\text{in}}$, where $A_{\text{fs}} = \int \frac{\epsilon(r)|E(r)|^2}{\max(\epsilon(r)|E(r)|^2)} d^2 r$ at the beam waist and $V_{\text{R6G,fs}} = t A_{\text{fs}}$, t being the thickness of the rhodamine 6G film on the substrate. Note that the ratio $\frac{V_{\text{R6G,fs}}}{A_{\text{fs}}}$ is simply t, but we write in this form to compare the result from WGM pumping of the microsphere.

The pump enhancement factor (F_{pump}) is the ratio between the collected Raman-scattered light intensity with WGM pumping to that with free-space pumping, without considering the Purcell effect. From the result above, ignoring the difference in collection efficiency between WGM pumping and free-space pumping, this ratio can be written as $F_{\text{pump}} = \frac{V_{\text{R6G,WGM}}}{V_{\text{R6G,fs}}} \frac{A_{\text{fs}}}{A_{\text{WGM}}} \frac{1}{2\pi} \frac{\Delta\lambda_{\text{FSR}}}{\Delta\lambda_{\text{FWHM}}} \eta_{\text{pump}}$.

For the silica microsphere that we used to collect the rhodamine 6G Raman spectrum, we have $D = 17.3$ μm, $\lambda_{\text{pump}} = 769.30$ nm, and $n = 1.45$. By considering the resonator to be a perfect sphere (ignoring eccentricity) and using the analytical equation for spherical resonators, we identify that the pump mode corresponds to a TE mode with mode numbers $n = 1$, $l = 95$, and $m = 95$, where n, l, and m are the radial, polar, and azimuthal mode number, respectively. This mode has a mode volume of 42.5 μm^3 and a mode cross section of $A_{\text{WGM}} = 0.817$ μm^2 [47]. By considering the rhodamine 6G coverage to be a 3.4 nm thin film on the microsphere surface, we estimate the effective volume of rhodamine 6G to be $V_{\text{R6G,WGM}} = 0.056$ μm^3. The free spectral range for this microsphere at the pump wavelength was calculated as $\Delta\lambda_{\text{FSR}} = \frac{\lambda_{\text{pump}}^2 \tan^{-1}(n^2-1)^{1/2}}{2\pi R(n^2-1)^{1/2}} = 8.4$ nm [42]. The linewidth was measured experimentally to be $\Delta\lambda_{\text{FWHM}} = 0.18$ pm, which corresponds to $Q = 4.3 \times 10^6$.

The term η_{pump} was estimated by monitoring the transmission through the tapered fiber coupler. η_{pump} was calculated as $\eta_{\text{pump}} = 1 - \frac{1}{T} \int_{t=0}^{t=T} \frac{P_{\text{coupled}}}{P_{\text{uncoupled}}} dt$, where $P_{\text{uncoupled}}$ is the transmitted power through tapered fiber coupler without the microsphere coupled, and $\frac{1}{T} \int_{t=0}^{t=T} P_{\text{coupled}} dt$ is the time averaged transmission through the tapered fiber coupler with the microsphere at critical coupling, as the pump laser wavelength is scanned with a triangle wave with period T. This factor represents the fraction of incident power coupled into the microsphere on average, and it accounts for the changing wavelength detuning, as the pump laser is scanned across the resonance mode, as well as any thermal shift in the resonance mode that changes the detuning. To demonstrate the validity of using η_{pump} as a correction factor, we recorded several different Raman spectra, as we change the wavelength scan range of the pump laser, which leads to different η_{pump}. The emitted Raman intensity was proportional to η_{pump} as expected (Fig. 5).

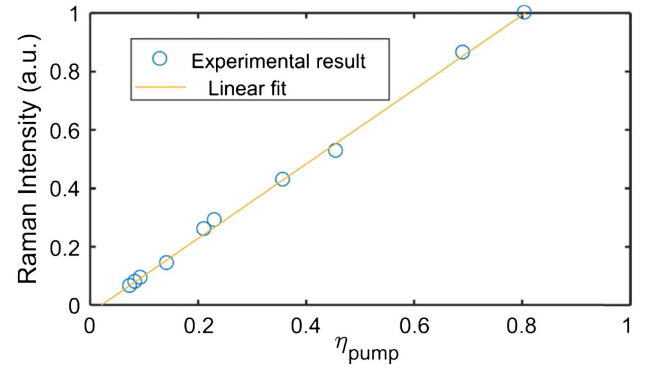For free-space pumping, the pump beam waist size was estimated to be $w_0 = 3.5$ μm in radius. This results in an

Fig. 5. Dependence of Raman intensity on η_{pump}. The wavelength scanning range of the pump laser was changed to obtain different η_{pump}.

effective excitation area of $A_{\text{fs}} = \frac{1}{2}\pi w_0^2 = 20$ μm^2. The effective excitation volume is found from $V_{\text{R6G,fs}} = A_{\text{fs}} \times t$, where $t = 200$ nm is the estimated thickness of rhodamine 6G film on the substrate, resulting in $V_{\text{R6G,fs}} = 4$ μm^3. Note that, in calculating the Raman scattered light intensity, we take the ratio $\frac{V_{\text{R6G,fs}}}{A_{\text{fs}}}$ and A_{fs} cancels out from the final expression; thus, an accurate estimation of the beam size is not important in the final result.

From our experiment, we obtained $V_{\text{R6G,WGM}} = 0.056$ μm^3, $V_{\text{R6G,fs}} = 4$ μm^3, $A_{\text{WGM}} = 0.817$ μm^2, $A_{\text{fs}} = 20$ μm^2, $\Delta\lambda_{\text{FSR}} = 8.4$ nm, $\Delta\lambda_{\text{FWHM}} = 0.18$ pm, and $\eta_{\text{pump}} = 0.47$. This results in $F_{\text{pump}} = 1204$.

APPENDIX B: CALCULATION OF THE PURCELL ENHANCEMENT FACTOR

The Purcell factor, in its most simplified form, is often written as $C = \frac{3}{4\pi^2} \lambda_s^3 \frac{Q_s}{V_s}$, where λ_s, Q_s, and V_s are the resonance wavelength, Q-factor, and mode volume of the Stokes WGM. When written this way, the Purcell factor represents the ratio of the emission rate into an optical cavity with unity refractive index to the emission ratio into free space. In our experiment, we need to compare the emission into a WGM with effective index n to the emission into free space, which results in an additional factor of $\frac{1}{n^2}$ from the dependence of emitter-field coupling on refractive index of the medium [53]. Throughout our work, the refractive index of silica was taken to be 1.45, and the effective index of the WGMs was taken as equal to the bulk refractive index of silica as an approximation.

For an emitter with emission linewidth comparable or larger than the linewidth of the cavity resonance, the Purcell factor no longer depends only on the Q-factor of the cavity resonance but rather it depends on both the cavity linewidth and the linewidth of the emission peak [43]. In the case of Raman scattering, the expression for the Purcell factor is modified by replacing Q_s with Q_{eff}, where Q_{eff} is defined as $Q_{\text{eff}} = \frac{Q_s Q_R}{Q_s + Q_R}$. Here Q_s is the Q-factor of the Stokes WGM and $Q_R = \frac{\lambda_s}{\Delta\lambda_R}$, where $\Delta\lambda_R$ is the linewidth of the Raman peak. When the linewidth of the Raman peak is much larger than the linewidth of cavity resonance, as in our case,

Q_{eff} is well approximated by Q_R. From the measured spectrum, we find that the linewidth of the 1510 cm^{-1} peak, appearing at $\lambda_s = 870$ nm, is $\Delta\lambda_R = 1.36$ nm. Thus, we obtain $Q_{\mathrm{eff}} = 640$.

The mode volume of the WGM was calculated from analytical expressions. There were two WGMs observed to overlap with the Raman peak at 1510 cm^{-1}, observed at $\lambda_s = 870$ nm. The exact mode numbers of these two WGMs is not clear. However, for a spherical resonator with $R = 8.65$ μm and $n = 1.45$, an optical mode with mode numbers $n = 1$, $l = 83$, and $m = 83$ and TE polarization exists at 874.35 nm, and we assume that this mode at 874.35 nm well approximates the spatial distribution and mode volume of both observed WGMs at 870 nm. The mode volume was calculated to be $V_s = 49.1$ μm^3 [47].

η_E accounts for the reduced optical field strength at the surface of the microsphere (where the rhodamine 6G dyes are) compared with the maximum field strength within the silica microsphere as well as the spatial overlap between the pump WGM and the Stokes WGM. When there is a single emitter in the cavity not located at the maximum of the cavity field, the ideal Purcell factor is modified by $\frac{|E_s(r)|^2}{\max(|E_s(r)|^2)}$, where $E_s(r)$ is the electric field of the Stokes mode [43,45]. For multiple emitters at different locations with different pump power at each emitter, a weighted average of $\frac{|E_s(r)|^2}{\max(|E_s(r)|^2)}$ is taken, where the weight is the pump power at each emitter. Thus, η_E can be obtained as

$$\eta_E = \frac{\int_{\mathrm{R6G}} |E_p(r)|^2 \frac{|E_s(r)|^2}{\max(|E_s(r)|^2)} \mathrm{d}^3 r}{\int_{\mathrm{R6G}} |E_p(r)|^2 \mathrm{d}^3 r},$$

where E_p is the electric field of the pump mode, and the integration is on the volume of rhodamine 6G only [43]. For the pump WGM with $n = 1$, $l = 95$, and $m = 95$ at 769.10 nm and the Stokes WGM with $n = 1$, $l = 83$, and $m = 83$ at 874.35 nm, we calculate η_E to be 0.1709.

η_λ accounts for any detuning between the Raman peak and the Stokes WGM as well as more than one WGM overlapping with the Raman peak [45]. In calculating Q_{eff}, we have assumed that there is exactly one WGM at the center of the Lorentzian Raman peak; any discrepancy between the experimental spectrum and this ideal case is accounted by η_λ. For a single WGM overlapping with the Raman peak, η_λ is equal to the intensity of the Raman peak at the WGM resonance wavelength relative to the maximum intensity of the Raman peak. For more than one overlapping WGM, the sum of η_λ for each WGM is taken as the total η_λ. For the spectrum obtained in our experiment (Fig. 4), the two WGMs are symmetrically located on the two sides of the Raman peak, with each of them contributing 0.79, and thus overall, $\eta_\lambda = 1.58$.

η_Ω accounts for the difference in the collection efficiencies between the Stokes light emitted directly into free space and the Stokes light emitted into a WGM and then scattered into free space. Although in both cases the Stokes light is collected with the same NA = 0.55 objective lens, the collection efficiencies are different because these two emissions have different angular divergence. Light emitted directly into free space has a dipolar emission pattern, while the emission from WGMs are on the equatorial plane of the microsphere, tangential to the edge of the microsphere and with a small angular divergence in the

polar direction. Because the dipolar emission and the emission from WGMs are uniform over 2π radians in the azimuthal direction in the far field, for comparison we can ignore the azimuthal dependence and only consider the difference in emission pattern in the polar direction. For the emission from WGM, we approximate the angular divergence in the polar direction to be equal to that of a Gaussian beam with waist size equal to the size of the WGM cross section; we calculate the angular divergence to be 0.31 radians. The objective lens has NA = 0.55, corresponding to a collection angle of 0.58 radians. Thus, almost all the emission from WGM is collected by the objective. On the other hand, only 66% of the dipolar emission falls within the collection angle of the objective. Thus, η_Ω, defined as the ratio of the collection efficiency of the WGM emission to that of the dipolar emission, is calculated as $1/0.66 = 1.5$.

Further, a factor of 2 goes into the expression for F_{Purcell} due to the twofold degeneracy of optical modes in the microsphere, from having both clockwise and counterclockwise modes. Another factor of 0.5 goes into the expression due to the coupling to the tapered fiber coupler; we assume critical coupling to the tapered fiber at Stokes wavelength, in which case half of the light emitted into the WGM is lost to the tapered fiber, and the other half is emitted into free space (and a fraction of this light is collected by the objective).

By considering all the factors mentioned above, we obtain the Purcell enhancement in our experiment, as presented in Eq. (3).

APPENDIX C: PHOTOBLEACHING OF RHODAMINE 6G

A gradual decrease in the intensities of rhodamine 6G Raman peaks was observed during the course of the experiment for WGM pumping, even though we use a small pump power of 37 μW (Fig. 6). On the other hand, for free-space excitation, no such change in Raman intensity was observed even for pump power greater than 1 mW. We believe the decrease in Raman intensity is due to photobleaching, even though we are not pumping at the absorption peak of rhodamine 6G. This photobleaching effect is only observed for WGM pumping because pump enhancement due to WGM greatly increases the local pump power for the rhodamine 6G molecules. This photobleaching effect was used to obtain an accurate Raman spectrum corresponding to that of rhodamine 6G only (without silica Raman peaks) by taking the difference between the measured spectrum before and after photobleaching [Fig. 4(b)]. This method results in more accurate removal of silica Raman scattering than background subtraction through curve fitting, which is crucial for accurate estimation of the Raman enhancement factor.

APPENDIX D: EFFECTIVE NUMBER OF MOLECULES EXCITED WITH WGM EXCITATION AND FREE-SPACE EXCITATION

We use the effective volume of rhodamine 6G excited under each pumping scheme to find the ratio of effective number of molecules. We have defined $V_{\mathrm{R6G,WGM}}$ and $V_{\mathrm{R6G,fs}}$

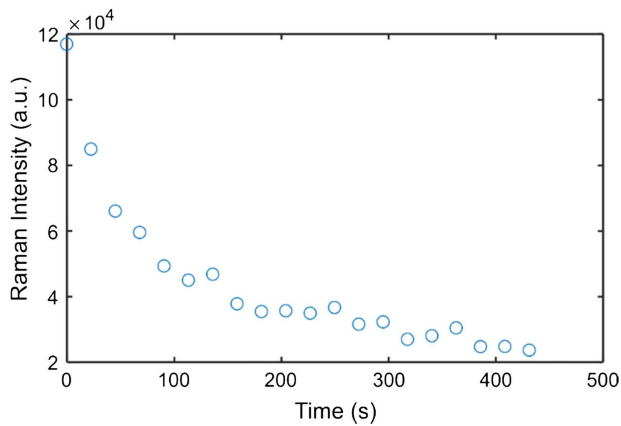**Fig. 6.** Change in Raman intensity as rhodamine 6G photobleaches. The pump power was 37 µW, coupled to the microsphere WGM through a tapered fiber.

previously to calculate the pump enhancement factor. These can be considered as the effective volume of rhodamine 6G being excited under each pumping scheme, with each differential volume of rhodamine 6G being normalized by the local pump power. $V_{\text{R6G,WGM}}$ and $V_{\text{R6G,fs}}$ corresponds to the volume of rhodamine 6G required at the electric field maximum, which would result in the same Raman intensity as the actual experiment. However, for the case of WGM pumping, the field maximum used for normalization is the maximum in the entire WGM modal distribution, which is located inside the silica sphere and cannot be reached by rhodamine 6G molecules. To be realistic, we must instead normalize by the field maximum on the surface of the microsphere. Thus, the ratio $\frac{N_{\text{SERS}}}{N_0}$ can be obtained as

$$\frac{N_{\text{SERS}}}{N_0} = \frac{V_{\text{R6G,WGM}} \times \frac{\max(|E_p(\mathbf{r})|^2)}{\max_{\text{surface}}(|E_p(\mathbf{r})|^2)}}{V_{\text{R6G,fs}}} = 0.065. \qquad \textbf{(D1)}$$

REFERENCES

1. F. Vollmer and S. Arnold, "Whispering-gallery-mode biosensing: label-free detection down to single molecules," Nat. Methods **5**, 591–596 (2008).
2. F. Vollmer and L. Yang, "Label-free detection with high-Q microcavities: a review of biosensing mechanisms for integrated devices," Nanophotonics **1**, 267–291 (2012).
3. L. He, S. K. Ozdemir, J. Zhu, W. Kim, and L. Yang, "Detecting single viruses and nanoparticles using whispering gallery microlasers," Nat. Nanotechnol. **6**, 428–432 (2011).
4. V. Dantham, S. Holler, C. Barbre, D. Keng, V. Kolchenko, and S. Arnold, "Label-free detection of single protein using a nanoplasmonic-photonic hybrid microcavity," Nano Lett. **13**, 3347–3351 (2013).
5. M. D. Baaske, M. R. Foreman, and F. Vollmer, "Single-molecule nucleic acid interactions monitored on a label-free microcavity biosensor platform," Nat. Nanotechnol. **9**, 933–939 (2014).
6. M. D. Baaske and F. Vollmer, "Optical observation of single atomic ions interacting with plasmonic nanorods in aqueous solution," Nat. Photonics **10**, 733–739 (2016).
7. L. Shao, X.-F. Jiang, X.-C. Yu, B.-B. Li, W. R. Clements, F. Vollmer, W. Wang, Y.-F. Xiao, and Q. Gong, "Detection of single nanoparticles and lentiviruses using microcavity resonance broadening," Adv. Mater. **25**, 5616–5620 (2013).
8. F. Vollmer, S. Arnold, and D. Keng, "Single virus detection from the reactive shift of a whispering-gallery mode," Proc. Natl. Acad. Sci. USA **105**, 20701–20704 (2008).
9. K. D. Heylman, N. Thakkar, E. H. Horak, S. C. Quillin, C. Cherqui, K. A. Knapper, D. J. Masiello, and R. H. Goldsmith, "Optical microresonators as single-particle absorption spectrometers," Nat. Photonics **10**, 788–795 (2016).
10. J. Zhu, S. K. Ozdemir, Y.-F. Xiao, L. Li, L. He, D.-R. Chen, and L. Yang, "On-chip single nanoparticle detection and sizing by mode splitting in an ultrahigh-Q microresonator," Nat. Photonics **4**, 46–49 (2009).
11. S.-Y. Ding, J. Yi, J.-F. Li, B. Ren, D.-Y. Wu, R. Panneerselvam, and Z.-Q. Tian, "Nanostructure-based plasmon-enhanced Raman spectroscopy for surface analysis of materials," Nat. Rev. Mater. **1**, 016021 (2016).
12. E. C. Le Ru, E. Blackie, M. Meyer, and P. G. Etchegoint, "Surface enhanced Raman scattering enhancement factors: a comprehensive study," J. Phys. Chem. C **111**, 13794–13803 (2007).
13. P. L. Stiles, J. A. Dieringer, N. C. Shah, and R. P. Van Duyne, "Surface-enhanced Raman spectroscopy," Annu. Rev. Anal. Chem. **1**, 601–626 (2008).
14. I. Alessandri and J. R. Lombardi, "Enhanced Raman scattering with dielectrics," Chem. Rev. **116**, 14921–14981 (2016).
15. M. Caldarola, P. Albella, E. Cortés, M. Rahmani, T. Roschuk, G. Grinblat, R. F. Oulton, A. V. Bragas, and S. A. Maier, "Non-plasmonic nanoantennas for surface enhanced spectroscopies with ultra-low heat conversion," Nat. Commun. **6**, 7915 (2015).
16. V. R. Dantham, P. B. Bisht, and C. K. R. Namboodiri, "Enhancement of Raman scattering by two orders of magnitude using photonic nanojet of a microsphere," J. Appl. Phys. **109**, 103103 (2011).
17. I. Alessandri, "Enhancing Raman scattering without plasmons: unprecedented sensitivity achieved by TiO$_2$ shell-based resonators," J. Am. Chem. Soc. **135**, 5541–5544 (2013).
18. I. Alessandri, N. Bontempi, and L. E. Depero, "Colloidal lenses as universal Raman scattering enhancers," RSC Adv. **4**, 38152–38158 (2014).
19. K. J. Yi, H. Wang, Y. F. Lu, and Z. Y. Yang, "Enhanced Raman scattering by self-assembled silica spherical microparticles," J. Appl. Phys. **101**, 063528 (2007).
20. C. L. Du, J. Kasim, Y. M. You, D. N. Shi, and Z. X. Shen, "Enhancement of Raman scattering by individual dielectric microspheres," J. Raman Spectrosc. **42**, 145–148 (2011).
21. M. S. Anderson, "Nonplasmonic surface enhanced Raman spectroscopy using silica microspheres," Appl. Phys. Lett. **97**, 131116 (2010).
22. N. Bontempi, L. Carletti, C. De Angelis, and I. Alessandri, "Plasmon-free SERS detection of environmental CO$_2$ on TiO$_2$ surfaces," Nanoscale **8**, 3226–3231 (2016).
23. D. Qi, L. Lu, L. Wang, and J. Zhang, "Improved SERS sensitivity on plasmon-free TiO$_2$ photonic microarray by enhancing light-matter coupling," J. Am. Chem. Soc. **136**, 9886–9889 (2014).
24. Y. Yan, C. Xing, Y. Jia, Y. Zeng, Y. Zhao, and Y. Jiang, "Self-assembled dielectric microsphere array enhanced Raman scattering for large-area and ultra-long working distance confocal detection," Opt. Express **23**, 25854–25865 (2015).
25. L. Yang, X. Jiang, W. Ruan, B. Zhao, W. Xu, and J. R. Lombardi, "Observation of enhanced Raman scattering for molecules adsorbed on TiO$_2$ nanoparticles: charge-transfer contribution," J. Phys. Chem. C **112**, 20095–20098 (2008).
26. Y. Wang, W. Ruan, J. Zhang, B. Yang, W. Xu, B. Zhao, and J. R. Lombardi, "Direct observation of surface-enhanced Raman scattering in ZnO nanocrystals," J. Raman Spectrosc. **40**, 1072–1077 (2009).
27. C. C. Evans, C. Liu, and J. Suntivich, "TiO$_2$ nanophotonic sensors for efficient integrated evanescent Raman spectroscopy," ACS Photon. **3**, 1662–1669 (2016).

28. D. H. Murgida and P. Hildebrandt, "Disentangling interfacial redox processes of proteins by SERR spectroscopy," Chem. Soc. Rev. **37**, 937–945 (2008).

29. M. Mahmoudi, S. E. Lohse, C. J. Murphy, A. Fathizadeh, A. Montazeri, and K. S. Suslick, "Variation of protein corona composition of gold nanoparticles following plasmonic heating," Nano Lett. **14**, 6–12 (2014).

30. D. R. Ward, D. A. Corley, J. M. Tour, and D. Natelson, "Vibrational and electronic heating in nanoscale junctions," Nat. Nanotechnol. **6**, 33–38 (2010).

31. A. Kuhlicke, S. Schietinger, C. Matyssek, K. Busch, and O. Benson, "In situ observation of plasmon tuning in a single gold nanoparticle during controlled melting," Nano Lett. **13**, 2041–2046 (2013).

32. L. K. Ausman and G. C. Schatz, "Whispering-gallery mode resonators: surface enhanced Raman scattering without plasmons," J. Chem. Phys. **129**, 054704 (2008).

33. R.-S. Liu, W.-L. Jin, X.-C. Yu, Y.-C. Liu, and Y.-F. Xiao, "Enhanced Raman scattering of single nanoparticles in a high-Q whispering-gallery microresonator," Phys. Rev. A **91**, 043836 (2015).

34. M. Cai and K. Vahala, "Highly efficient optical power transfer to whispering-gallery modes by use of a symmetrical dual-coupling configuration," Opt. Lett. **25**, 260–262 (2000).

35. Ş. K. Özdemir, J. Zhu, X. Yang, B. Peng, H. Yilmaz, L. He, F. Monifi, S. H. Huang, G. L. Long, and L. Yang, "Highly sensitive detection of nanoparticles with a self-referenced and self-heterodyned whispering-gallery Raman microlaser," Proc. Natl. Acad. Sci. USA **111**, E3836–E3844 (2014).

36. J.-B. Jager, V. Calvo, E. Delamadeleine, E. Hadji, P. Noé, T. Ricart, D. Bucci, and A. Morand, "High-Q silica microcavities on a chip: from microtoroid to microsphere," Appl. Phys. Lett. **99**, 181123 (2011).

37. X. Jiang, M. Wang, M. C. Kuzyk, T. Oo, G.-L. Long, and H. Wang, "Chip-based silica microspheres for cavity optomechanics," Opt. Express **23**, 27260–27265 (2015).

38. M. Tomes and T. Carmon, "Photonic micro-electromechanical systems vibrating at X-band (11-GHz) rates," Phys. Rev. Lett. **102**, 113601 (2009).

39. T. J. Kippenberg, S. M. Spillane, B. Min, and K. J. Vahala, "Theoretical and experimental study of stimulated and cascaded Raman scattering in ultrahigh-Q optical microcavities," IEEE J. Sel. Top. Quantum Electron. **10**, 1219–1228 (2004).

40. T. Carmon, L. Yang, and K. J. Vahala, "Dynamical thermal behavior and thermal self-stability of microcavities," Opt. Express **12**, 4742–4750 (2004).

41. M. L. Gorodetsky and V. S. Ilchenko, "Optical microsphere resonators: optimal coupling to high-Q whispering-gallery modes," J. Opt. Soc. Am. B **16**, 147–154 (1999).

42. R. Symes, R. M. Sayera, and J. P. Reid, "Cavity enhanced droplet spectroscopy: principles, perspectives and prospects," Phys. Chem. Chem. Phys. **6**, 474–487 (2004).

43. X. Checoury, Z. Han, M. El Kurdi, and P. Boucaud, "Deterministic measurement of the Purcell factor in microcavities through Raman emission," Phys. Rev. A **81**, 033832 (2010).

44. B. Petrak, N. Djeu, and A. Muller, "Purcell-enhanced Raman scattering from atmospheric gases in a high-finesse microcavity," Phys. Rev. A **89**, 023811 (2014).

45. H. Kaupp, C. Deutsch, H. C. Chang, J. Reichel, T. W. Hansch, and D. Hunger, "Scaling laws of the cavity enhancement for nitrogen-vacancy centers in diamond," Phys. Rev. A **88**, 053812 (2013).

46. T. Hümmer, J. Noe, M. S. Hofmann, T. W. Hänsch, A. Högele, and D. Hunger, "Cavity-enhanced Raman microscopy of individual carbon nanotubes," Nat. Commun. **7**, 12155 (2016).

47. S. Balac and P. Féron, "Whispering gallery modes volume computation in optical micro-spheres," Research Report <hal-01279396>, FOTON, 2014, https://hal.inria.fr/FOTON_SYSPHOT/hal-01279396v1.

48. Ş. K. Özdemir, J. Zhu, L. He, and L. Yang, "Estimation of Purcell factor from mode-splitting spectra in an optical microcavity," Phys. Rev. A **83**, 033817 (2011).

49. M. Pelton, "Modified spontaneous emission in nanophotonic structures," Nat. Photonics **9**, 427–435 (2015).

50. B. L. Darby, P. G. Etchegoin, and E. C. Le Ru, "Single-molecule surface-enhanced Raman spectroscopy with nanowatt excitation," Phys. Chem. Chem. Phys. **16**, 23895–23899 (2014).

51. P. G. Etchegoin, E. C. Le Ru, and M. Meyer, "Evidence of natural isotopic distribution from single-molecule SERS," J. Am. Chem. Soc. **131**, 2713–2716 (2009).

52. E. L. Ru and P. Etchegoin, *Principles of Surface-Enhanced Raman Spectroscopy: and Related Plasmonic Effects* (Elsevier, 2008).

53. M. Scully and M. S. Zubairy, *Quantum Optics* (Cambridge University, 1997).